Influence of fluid viscosity hierarchy on the reverse-circulation displacement efficiency

Maryam Ghorbani [a,*], Knut Erik Teigen Giljarhus [b], Hans Joakim Skadsem [a]

[a] Department of Energy and Petroleum Technology, University of Stavanger, Stavanger, 4036, Norway
[b] Department of Mechanical and Structural Engineering and Materials Science, Stavanger, 4036, Norway

ARTICLE INFO

ABSTRACT

Reverse-circulation cementing is an alternative strategy for well cementing where the cementing fluids are injected directly into the annulus from the surface. This cementing strategy can reduce downhole circulation pressures compared to conventional circulation cementing and potentially eliminate the need for retarders in the cement slurry. In reverse-circulation operations, the fluid hierarchy will normally involve density-unstable combinations along the annulus. Since the annular geometry prevents the mechanical separation of fluids, reverse-circulation cementing is associated with a risk of slurry contamination and mixing during placement. Although reverse-circulation cementing has been known for several decades and is used for cementing of both onshore and offshore wells, it remains unclear whether conventional circulation job design guidelines apply to reverse-cementing or indeed how fluid properties should be optimized for such operations. The purpose of the current study is to contribute to the understanding of buoyant annular displacements, with a particular focus on the role of viscosity hierarchy on the annular displacement in vertical and near-vertical annuli.

We present a combined experimental and numerical study of density-unstable downward displacements in a downscaled, narrow concentric annulus. A transparent annulus flow loop was used to conduct downward displacements. A high-speed camera and a mirror arrangement were used to track the displacement. Numerical simulations of the experiments and selected other cases were performed using the open-source OpenFOAM computation framework. We study Newtonian and mildly shear-thinning fluids, and our study aims to determine whether it is more efficient to use a displacing fluid with higher viscosity or lower viscosity than the displaced fluid while maintaining a constant average viscosity for the fluid pair. The experimental and numerical results, which are in good qualitative agreement, demonstrate that the viscosity hierarchy of the fluids significantly affects the displacement flow features. Our results show that a more viscous displaced fluid leads to faster growth of the instabilities and, as a result, less efficient displacement. Oppositely, we observe less tendency for finger growth and a more diffusive mixing region for more viscous displacing fluids. The effect of the viscosity hierarchy can get stronger by increasing the inclination of the annulus and the viscosity difference between the fluids from 0.006 to about 0.02 Pa·s. The findings can assist in the selection of fluid properties for future reverse-circulation displacement operations.

1. Introduction

Oil & gas wells and wells for geothermal energy recovery or geological carbon storage are constructed by first drilling through overburden rock formations and subsequently running a casing string or liner that is cemented to the newly drilled formation. The overburden needs to be drilled in stages or sections due to different stress and pressure gradients inside the wellbore and in the surrounding formation. That is, the drilling fluid in the wellbore can only balance formation collapse and fracture pressure over a limited depth-interval before a casing string needs to be run and cemented to the formation. Primary cementing

is normally performed by pumping cementing fluids and wiper plugs down the well inside the string that is to be cemented; the fluids exit the string at the bottom of the well to displace the original drilling fluid from the annular space between the string and the newly drilled formation (Nelson and Guillot, 2006). Once hardened, the casing and annular cement sheath isolate the weaker formations above and allow increasing the density of the drilling fluid for drilling of the next, deeper section (Fjær et al., 2008).

Since cement slurries and spacer fluids are normally denser and more viscous than the original drilling fluid in the well, the total

pressure exerted onto the newly drilled formation increases as the cementing fluids are placed behind the casing string or liner. Narrow margins between collapse or pore pressure and the fracture pressure along the open-hole section may place restrictions on the allowable density of the cement slurry, the total height of cement placed behind casing, the placement pumping rate (Nelson and Guillot, 2006), or necessitate a staged cementing strategy that utilizes stage collars or external casing packers (Turki and Mackay, 1983).

An alternative strategy for reducing the total pressure load on the rock formation is to inject cementing fluids from the surface and directly into the annulus that is to be cemented. This strategy, which has been deployed at least since the mid-1960s and is often referred to as reverse-circulation cementing, can lead to significant reductions in the circulating pressure close to the bottom of the hole (Marquairi and Brisac, 1966). The reduction in circulating pressure is attributed to the lower friction pressure gradient inside the casing compared to along the narrow annulus between casing and formation and the observation that the bottom-hole pressure is the sum of the hydrostatic component and the friction pressure loss beyond the point of consideration, *i.e.*, inside the casing (along the annulus) for reverse-circulation (conventional) cementing operations (Marquairi and Brisac, 1966; Davies et al., 2004; Macfarlan et al., 2017). The reduced pressure may enable the use of denser cement slurries and/or placing the cement slurry at a higher flow rate, which reduces the time required for cementing and has been reported in the past to be beneficial for mud displacement (Marquairi and Brisac, 1966). Finally, since the cement slurry is placed directly into the annulus and does not circulate through the casing first, reverse-circulation reduces the need for retarders in the cement slurry (Hernández and Bour, 2010; Wreden et al., 2014).

Reverse-circulation cementing operations have been performed extensively since the case study by Marquairi and Brisac (1966), and published records include several onshore wells, *e.g.* on the west coast of the United States (Hernández and Bour, 2010) and at the Reykjanes peninsula, Iceland (Friðleifsson et al., 2017), in addition to offshore in the Gulf of Mexico (MacEachern et al., 2003) and the Beaufort Sea (Marriott et al., 2007). The potential for reduction in circulation pressure during cementing means that the method is relevant for well construction in areas with lost-circulation zones (Moore et al., 2005; Hernandez, 2012). For potential deepwater applications and wells with a subsea wellhead, a switchable crossover tool has been developed that allows injecting cementing fluids from the surface to the top of the casing annulus via a working string (Grant et al., 2014; Murdoch et al., 2016; Reagins et al., 2016). Injecting (bullheading) cement slurry into the annulus from the surface is also sometimes done to cement above a loss zone; a recently studied example includes the North Sea production well discussed by Skadsem et al. (2021). The well was constructed in 1985, and the 9 5/8-in production casing was cemented in two stages: first, conventionally up to the weak formation (performed without returns), followed by an injectivity test and bullheading of cement slurry down the annulus. Subsequent characterization of casing and cement sections retrieved during the abandonment of the well showed some contamination in the form of barite intrusions and apparent mud remains along the casing walls (Beltrán-Jiménez et al., 2022), but also shorter intervals of moderately-bonded, low-permeable annulus cement (Skadsem, 2022). A similar cementing strategy is referred to as the bradenhead cementing method, and this method also involves the second-stage downward displacement of mud by cementing fluids, as recently discussed by Pelton et al. (2023). Their study, which was based on more than 50 jobs in the Greater Permian basin, demonstrated the usefulness of a second-stage downward displacement when the well presents a possible injection point that can receive fluids bullheaded from the surface (Pelton et al., 2023). Although the cementing operation is not referred to as *reverse-circulation* cementing, the second-stage in a bradenhead cementing operation presents similar annular displacement conditions as a reverse-circulation operation.

Whereas the above examples discussed relatively successful reverse-circulation operations, certain technical and physical aspects of these operations pose challenges pertaining to this placement strategy. In conventional circulation cementing, pumping stops when the internal top plug lands at the bottom of the casing, and float equipment will prevent fluids from flowing back into the casing until the cement has hardened. In reverse-circulation operations, it is more difficult to determine *when* the cement slurry has reached the bottom of the well and starts flowing into the casing, and conventional float equipment is not compatible with this circulation direction (Hernández and Bour, 2010). Furthermore, due to the particular fluid hierarchy involved in reverse-circulation jobs, the cement slurry that is pumped *first* downhole is the cement that should end up sealing around the casing shoe. Since the shoe cement is pumped first in reverse-circulation operations, there is an increased risk of contaminating this part of the annular cement compared to conventional circulation (where the shoe cement is the last slurry pumped down the well). The risk of contamination is likely to increase for denser cement slurries since it is not possible to mechanically separate fluids while placing them in the annulus (Wreden et al., 2014). Contamination problems were indicated by Bour et al. (2013) as a possible explanation for the relatively high top-of-cement inside the casing following a reverse-circulation cementing operation in Australia.

The challenges introduced above, namely the practical difficulty of separating successive fluids during placement and the risk of contaminating the shoe cement, motivate further study of downward annular fluid displacement. An initial study by Wreden et al. (2014) focused on the fluid-fluid interface between a dense shoe slurry that was displaced downward by a lighter "lead" slurry. Their observations showed that it is possible to avoid or minimize mixing between the slurries provided the "lead" slurry is made more viscous than the denser shoe slurry below (Wreden et al., 2014). From the perspective of interface stability, this configuration corresponds to a density-stable and viscosity-stable hierarchy (lighter, more-viscous fluid displacing denser, less-viscous fluid downward) and reverses the typical viscosity hierarchy associated with effective laminar displacement design rules (Couturier et al., 1990; Pelipenko and Frigaard, 2004). The purpose of the current study is to perform a similar analysis, but now focusing on the critical interface between the shoe cement and the spacer or drilling fluid below. Since, as pointed out above, the shoe cement is often considered the most critical part of the annular cement column, the shoe cement slurry is often also *denser* than the other fluids involved in the cementing operation (Nelson and Guillot, 2006). As such, we deliberately study a density-unstable fluid hierarchy and examine how the viscosity hierarchy and annular inclination impact displacement efficiency. While we center the discussion on reverse-circulation *cementing* operations, similar fluid hierarchies and technical challenges can also be relevant for wellbore clean-out operations in the context of well completions, such as those discussed in the study of McNerlin et al. (2013).

Due to the significance and importance of well cementing operations, fluid displacement problems have been examined in the past both in pipe and annular geometries, at varying inclinations and flowing conditions, and using both experimental and theoretical or numerical methods. The majority of previous research has focused on *conventional* circulation operations, corresponding to the downward flow of cementing fluids inside the casing string and an upward flow in the annulus outside the casing. Previous work on buoyant downward displacements has frequently considered pipe geometries and has been motivated by studying the displacement and mixing of cementing fluids inside the casing and in the absence of wiper plugs. Displacements have been categorized as instantaneous (*i.e.* displacements without backflow of lighter fluid), diffusive, viscous, or inertial (Alba et al., 2013). Recent experiments and three-dimensional numerical simulations of such buoyant displacement flows have been in good agreement, and it has been found that viscosity-stable configurations (*i.e.* displacing fluid is more viscous than the displaced fluid) generally improve displacement

efficiency in pipe geometries (Etrati et al., 2018; Etrati and Frigaard, 2018).

Reverse-circulation displacements in annular geometries have been studied to a lesser extent, but a recent experimental research effort by Eslami et al. (2022) investigated the effects of viscosity ratio, buoyancy, imposed flow, eccentricity, and casing reciprocation in a vertical annulus. Their study considered the displacement of a Newtonian, shear-thinning, or viscoplastic fluid by a Newtonian fluid and covered a wide range of imposed flow rates. In the density-unstable configuration, their results demonstrated a transition from partial mixing for iso-viscous fluid pairs to strong interfacial (viscous fingering) instabilities when the displacing fluid was considerably less viscous compared to the displaced fluid (Eslami et al., 2022). Strong suppression of viscous fingering instabilities was observed when the fluid hierarchy was made density-stable, for which gravity acts to preserve a horizontal interface between the fluids (Wreden et al., 2014); this particular fluid configuration can be linked to a less dense "lead" cement slurry displacing the denser shoe slurry downward, as investigated by Wreden et al. (2014). The experimental study of Eslami et al. (2022) identified density difference, eccentricity, and casing reciprocation to have the strongest impact on the displacement, with eccentricity resulting in potentially static fluid along the narrow side in the case of a displaced fluid with viscoplastic behavior. Another recent study of reverse-circulation displacement in a vertical annulus geometry was reported by Ghorbani et al. (2023), who combined experiments and computational fluid dynamics with a focus on the concentric annulus. Similar to Eslami et al. (2022), displacements involving density-unstable fluid pairs were found to be inherently unstable; increasing the imposed, downward flow rate was seen to "stabilize" the displacements in the sense that upward (backflow) of the lighter fluid was reduced. Drawing on previous experiments in pipe geometries (Debacq et al., 2001; Alba et al., 2013), the spreading of the fluid-fluid interface was found to spread according to a diffusive (inverse square root of time) scaling (Ghorbani et al., 2023).

The current study generalizes the previous effort by Ghorbani et al. (2023) in two important directions: we study (i) the effect of viscosity hierarchy is considered while maintaining a fixed average viscosity across the two fluids, and (ii) the effect of inclination on density-unstable reverse-circulation displacements. The results can guide fluid design for future reverse-circulation displacement operations, with an emphasis on the role played by the fluid viscosity hierarchy. We explore density-unstable displacements with different fluid viscosity hierarchies in a concentric and vertical annulus experimentally, using a transparent annulus test fixture, and compare them to numerical results from 3-dimensional computational fluid dynamics simulations. We subsequently explore the effects of annulus inclination on displacement efficiency within different sectors of the annular cross section by additional numerical simulations.

2. Methodology

In the following we present the experimental and computational methods used to explore density-unstable annular displacements. The experimental test setup and the visualization technique used for tracking the fluid-fluid interface are presented in Section 2.1. We proceed by defining relevant dimensionless numbers that characterize the annular geometry and the balance between relevant forces that affect the displacement experiments in Section 2.1.2. We will subsequently return to the topic of scaling while discussing implications of our observations in Section 5. The computational method is discussed in detail in Section 2.2.
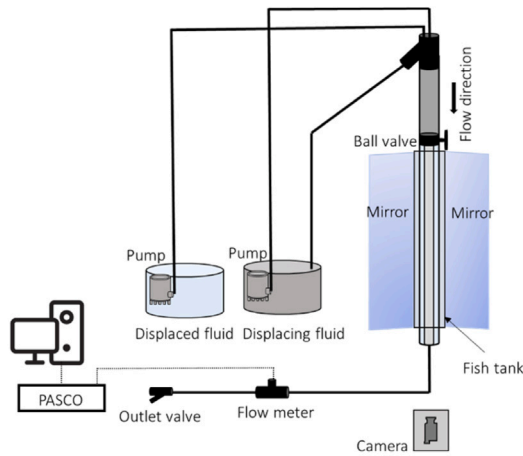
2.1. Experiments

Displacement experiments were performed using an annular flow loop consisting of an outer transparent pipe with an inner diameter of $D_o = 40$ mm and an inner opaque pipe with an outer diameter of $D_i = 25$ mm. The flow loop has previously been presented by Ghorbani et al. (2023), but relevant details will be repeated below for completeness. Inner pipe centralization was achieved using two rigid centralizers fitted on the top and bottom of the inner pipe. A manual ball valve ensured the initial separation of the two fluids. The annular test section is 1500 mm long, corresponding to 100 hydraulic diameters, $D_h = D_o - D_i$.

A schematic of our experimental setup is shown in Fig. 1(a). In preparation for an experiment, a pump was used to fill the annulus with displaced fluid from the bottom and up to the ball valve. After closing the ball valve, the denser displacing fluid was pumped to fill the rest of the test rig. At the inlet to the annular test section, an arrangement consisting of an overflow tank ensured a constant vertical liquid level throughout each experiment. A manual choke valve at the outlet was regulated to produce different magnitudes of imposed flow. A flowmeter was fitted to the outlet to control the imposed flow rate.

To visualize the flow, black ink was added to the displacing fluid. A Nikon D5500 camera operating at 60 frames per second was used to capture images of the experiments. The camera was placed in front of the test rig. A rectangular tank ("fish tank") filled with glycerol was attached outside the annular test section to improve the imaging of the fluids. To allow simultaneous imaging of the annulus from three directions, two mirrors were oriented at 45° angles as measured from the sides of the rectangular tank. The camera and mirror arrangement is shown in Fig. 1(b). Using reference marks on the fish tank, the reflected images in the mirrors were calibrated according to the direct optical view. We conducted all experiments in a dark room equipped with black curtains to eliminate stray light and reflections coming off other equipment. We employed two LEDs for illumination. One was in the back of the fish tank, and the other one was on the ground. The LED on the ground caused slightly non-uniform illumination along the annulus, which was adjusted by image post-processing. We conducted image processing using scripts written in Python, where the light intensity at each pixel, I, is normalized between 0 and 1 according to $I_N = (I - I_{Max})/(I_{Min} - I_{Max})$. I_{Max} is the light intensity of the pure displaced fluid, and I_{Min} represents the light intensity of an image of the rig fully filled with dyed displacing fluid. The light intensity of each pixel can be considered equivalent to the concentration of the displacing fluid, where the displacing fluid corresponds to $I_N \sim C = 1$, and the displaced fluid is taken as $I_N \sim C = 0$. The displacement experiments have been analyzed by visual inspection of the raw images, but also in the form of spatiotemporal diagrams and displacement efficiency curves. Spatiotemporal diagrams have been constructed by averaging the fluid concentration over the annulus cross-section and plotting the resulting axial concentration profile as a function of time since the beginning of the experiment. Finally, displacement efficiency curves have been prepared by calculating and plotting the volume fraction of displacing fluid inside the annulus as a function of time since the start of the experiment (Tehrani et al., 1993).

2.1.1. Fluids

The density-unstable displacement experiments were conducted using plain tap water and tap water with 3 different concentrations of xanthan gum (0.15 g/l, 0.3 g/l, 0.5 g/l) to produce more viscous, shear-thinning liquids. In all cases, sodium chloride was added to the displacing liquid at a concentration of 10 g/l to produce a density-unstable condition in the reverse-circulation configuration. The density and viscosity of the test fluids were measured using an Anton Paar DMA 4500 M density meter and an Anton Paar MCR 302 rheometer equipped with a concentric cylinder measurement geometry. The smooth-walled CC-27 measurement system were used for measuring the fluid viscosity;

(a) Schematic of the experimental set-up.
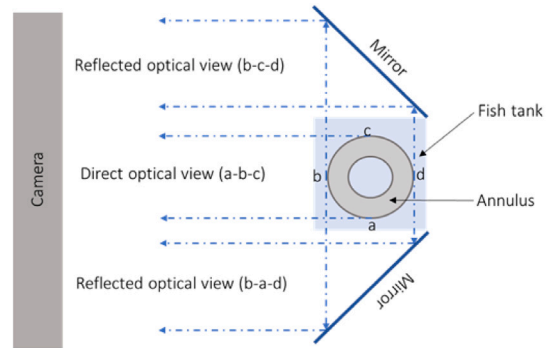
(b) Illustration of mirror arrangement for simultaneously imaging the full annular cross-section.

Fig. 1. Reverse-circulation displacement experiments were carried out in a vertical and concentric annular test rig (a) comprised of a transparent outer pipe that, combined with a mirror arrangement, enabled visualization of the full annular cross-section in a single frame (b).
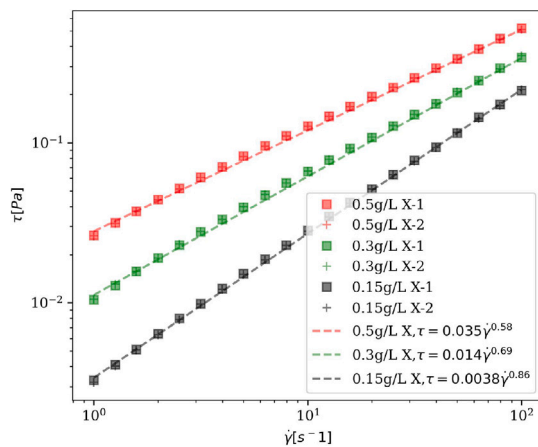

Fig. 2. Flow curves of Xanthan gum solution. The dashed lines represent the Power law fits. 1 and 2 represent two measurements.

this system consists of a rotating bob of diameter 26.653 mm, a cup with inner diameter 28.910 mm and a vertical measurement gap length of 40.032 mm. The viscosity of the fluids was measured over a shear rate interval from $1 \ s^{-1}$ to $100 \ s^{-1}$ using a shear rate-controlled measurement protocol. We note that wall-slip may affect the fluid flow curve measurement at low shear rates in smooth measurement geometries, such as that used here. Experimental observations of slip at the walls of a Hele-Shaw cell were recently reported by Abedi et al. (2022), who studied the displacement of a yield stress liquid by air in a radial configuration. Since the local shear rate decreases with radial distance from the origin (*i.e.* the injection point) in this geometry, fluids can become susceptible to wall-slip beyond a critical distance from the injection point. For the current concentric annular geometry and for the relatively diluted concentrations of polymer used in our test fluids, we do not expect wall-slip to significantly impact the buoyant displacements in the current study, or our interpretation of them. To a very good approximation, we find that the test fluids can be considered as time-independent generalized Newtonian fluids. We finally acknowledge that our model test fluids are simpler fluids than realistic wellbore and cementing fluids, which generally are suspensions consisting of weighting particles or cement particles, and that have thixotropic behavior (Skadsem et al., 2019) (see Fig. 2).

An overview of the fluid properties is provided in Table 1, where the viscosity, μ of the xanthan gum solutions is described by the power law

model, *i.e.* $\mu(\dot{\gamma}) = k\dot{\gamma}^{n-1}$, with k and n the consistency index and shear thinning index, respectively, and $\dot{\gamma}$ the shear rate (Bird et al., 1987). The Newtonian limit is obtained with $n \to 1$. The subscripts H and L in Table 1 refer to the properties of the displacing fluid (heavy) and displaced fluid (light), respectively.

2.1.2. Scaling

Since displacement experiments were performed in a downscaled annulus flow loop, we next consider the main dimensionless numbers that govern the displacements. We identify the annulus aspect ratio, $\kappa = D_i/D_o$, defined as the diameter ratio of the inner and outer pipes that form the annulus, annulus inclination, and inner pipe eccentricity as the main geometric features of the annular displacements. In experiments, we fixed the inclination to vertical (*i.e.* 0° inclination angle from vertical) and limited the study to the concentric annulus. The aspect ratio of the flow loop is 0.63, which is considered to be somewhat lower than typical casing-hole diameters for primary cementing operations (0.7–0.8). The current aspect ratio was chosen in part to improve image acquisition during displacement experiments (the annular clearance is slightly wider than typical wellbore annuli).

Further, we identify viscous, buoyant, and inertial stresses as relevant for the displacement experiments. Thus, the ratio of inertial to viscous stresses is reflected by the Reynolds number, $Re = \bar{\rho}V_0 d/\bar{\mu}$, which is based on the imposed flow velocity, V_0, the radial gap, $d = (D_o - D_i)/2$, the average fluid mass density, $\bar{\rho} = (\rho_H + \rho_L)/2$, and the geometric mean of the two (effective) viscosities, $\bar{\mu} = \sqrt{\mu_{\text{eff},H}\mu_{\text{eff},L}}$. To assess the effective viscosity of fluid i, we define $\mu_{\text{eff},i} = k_{p,i}\dot{\gamma}_N^{n-1}$, where $\dot{\gamma}_N = 3V_0/d$, and $k_{p,i} = \left[(2n+1)/3n\right]^n k_i$. This also allows us to define the (effective) viscosity ratio, $m = \mu_{\text{eff},L}/\mu_{\text{eff},H}$. In the remainder, we will refer to cases with $m > 1$ as *viscosity-unstable* conditions since now the displacing fluid is (effectively) less viscous than the displaced fluid. Finally, the ratio of inertial to buoyant stresses is quantified by the densimetric Froude number, $Fr = V_0/\sqrt{Atgd}$, where also the Atwood number is introduced as $At = (\rho_H - \rho_L)/(\rho_H + \rho_L)$.

Experiments were performed using fluid pairs with fixed density difference (*i.e.* fixed At) and at two different imposed flow velocities of 0.012 m/s and 0.025 m/s. The imposed flow velocity impacts the effective viscosity of the xanthan gum solution and, in turn, affects the Reynolds number and viscosity ratio. The complete test matrix for the experiments is provided in Table 2. As is seen from the table, the experiment conditions have been chosen to explore both viscosity-stable and -unstable configurations under the same Reynolds number (*e.g.* cases 1 and 3 both correspond to $Re \approx 19$–20, while m is varied from 0.05 to 23). Also presented in the table is a buoyant velocity scale,

Table 1
Fluid properties. All fluids are water-based and mixed with salt (S) or Xanthan gum (X).

Case	Displacing fluid (H)	ρ_H (kg/m^3)	k_H (Pa s^n)	n_H	Displaced fluid (L)	ρ_L (kg/m^3)	k_L (Pa s^n)	n_L
1,2	0.5 g/L X + 10 g/L S	1004	0.035	0.58	Water	998	0.001	1
3,4	10 g/L S	1004	0.001	1	0.5 g/L X	998	0.039	0.58
5,6	0.3 g/L X + 10 g/L S	1004	0.0123	0.71	Water	998	0.001	1
7,8	10 g/L S	1004	0.001	1	0.3 g/L X	998	0.014	0.69
9,10	0.15 g/L X + 10 g/L S	1004	0,0038	0.86	0.15 g/L X	998	0,0044	0.85

Table 2
Experimental test matrix.

Case	$\mu_{\text{eff},H}$ (Pa s)	$\mu_{\text{eff},L}$ (Pa s)	V_0 (m/s)	$\bar{\mu}$ (Pa s)	At	Fr	Re	m	V_b (m/s)
1	0.0205	0.001	0.012	0.0045	0.003	0.04	19.89	0.05	0.061
2	0.0151	0.001	0.025	0.0039	0.003	0.09	48.33	0.07	0.071
3	0.001	0.023	0.012	0.0048	0.003	0.04	18.84	22.88	0.057
4	0.001	0.017	0.025	0.0041	0.003	0.09	45.78	16.81	0.067
5	0.0085	0.001	0.012	0.0029	0.003	0.04	30.82	0.12	0.095
6	0.007	0.001	0.025	0.0026	0.003	0.09	71.42	0.14	0.106
7	0.001	0.0095	0.012	0.0031	0.003	0.04	29.26	9.48	0.089
8	0.001	0.0075	0.025	0.0027	0.003	0.09	68.31	7.55	0.102
9	0.0032	0.0036	0.012	0.0034	0.003	0.04	29.39	1.14	0.081
10	0.0029	0.0032	0.025	0.0031	0.003	0.09	61.15	1.14	0.089

V_b. We assess this velocity scale by balancing the pressure gradient due to buoyancy, $(\rho_H - \rho_L)g = \Delta\rho g$, by the friction pressure gradient associated with the mean viscosity, *i.e.* $12\bar{\mu}V_b/d^2$, where the concentric annulus has been approximated by a plane slot, for simplicity. That is, $V_b = \Delta\rho g d^2/(12\bar{\mu})$. For all cases in Table 2, the buoyant velocity scale exceeds the imposed velocity, which suggests that buoyancy-induced instabilities are expected to be important in all of these cases.

2.2. Computations

We performed 3-D numerical simulations of the fluid-fluid displacement in the annulus using OpenFOAM, version 2012, employing the twoLiquidMixingFoam solver. The twoLiquidMixingFoam solver is for two-phase, incompressible, and miscible fluids. The concentration is determined by a mixture fraction equation,

$$\frac{\partial C}{\partial t} + \nabla \cdot (CU) = 0, \tag{1}$$

where $C \in [0, 1]$ is the volumetric phase fraction of the displacing fluid. We assume molecular mixing between the fluids is negligible (Moore et al., 2005; Murdoch et al., 2016). The momentum and continuity equations are as follows:

$$\frac{\partial \rho U}{\partial t} + \nabla \cdot (\rho UU) = -\nabla p + \nabla \cdot 2\mu S + \rho g, \tag{2}$$

$$\nabla \cdot U = 0, \tag{3}$$

where $S = [(\nabla U) + (\nabla U)^T]/2$ is the rate of strain tensor, and g is the gravitational acceleration. The density and viscosity of the fluid can be found from the phase fraction as $\rho = C\rho_H + (1 - C)\rho_L$ and $\mu = C\mu_H + (1 - C)\mu_L$. The viscosity was modeled as a power law fluid with the measured properties given in Table 1. To ensure numerical stability at low shear rates, a maximum viscosity was defined as the viscosity obtained at $\dot{\gamma}_0 = 0.01$ 1/s.

Second-order discretization schemes and a second-order implicit scheme were employed for spatial terms and time discretization, respectively. To stabilize the solution, an adjustable time step with a maximum Courant number of 0.5 was used. For the boundary conditions, velocity Dirichlet conditions were prescribed at solid boundaries (no slip) and at the inlet (uniform velocity), and a Neumann outflow condition was applied at the outlet. For the pressure, Neumann inlet

and Dirichlet outlet conditions were used. A computational domain with a 1.5 m length, equal to 100 hydraulic diameters, in the axial direction was used. The initial interface between the two fluids was 0.5 m below the inlet at the top. The computational grid was a structured grid stretched towards the walls. The computational mesh consisted of 120 grid cells in the azimuthal direction, 22 cells in the radial direction, and 700 cells in the axial direction. The computational grid is shown in Fig. 3.

3. Experimental results

We next present experimental results obtained using the vertical and concentric annular test rig. We discuss the effects of the viscosity hierarchy, *i.e.* viscosity-stable, iso-viscous, and viscosity-unstable conditions, in Section 3.1. We note that the mean viscosity is approximately equal for these experiments, which means that the Reynolds number is constant across the experiments. We continue with the study of the effect of the viscosity ratio between displacing and displaced fluids for the same viscosity hierarchy in Section 3.2. We will next compare the results of the experimental and numerical modelings in Section 4, where we also address the effect of viscosity ratio in inclined annuli.

3.1. Effect of viscosity hierarchy (m) for fixed mean viscosity ($\bar{\mu}$)

Fig. 4 compares the annular displacements for cases 6, 10, and 8 in Table 2, corresponding to an imposed velocity of 0.025 m/s, a constant mean viscosity of approximately 0.0027–0.003 Pa s in all cases, but with different viscosity hierarchy, m. Cases 6, 10, and 8 correspond to viscosity-stable ($m < 1$), iso-viscous ($m = 1$), and viscosity-unstable ($m > 1$) cases, respectively. The images in the top row show the front view of the density unstable displacement along the annulus over time (at similar instances in the time since the start of the experiment, approximately 5 s apart). The front images clearly indicate the growth of the Rayleigh–Taylor instability due to the density unstable hierarchy of the fluids.

The diagrams in the second row show the corresponding spatiotemporal plots. In these, and in all subsequent plots, we let Z be the axial coordinate along the annulus, with $Z = 0$ m corresponding to the outlet and $Z = 0.7$ m as the interface position at the start of the experiment. The dashed curves in the spatiotemporal diagrams indicate the front position during the displacement at the bottom of the mixing zone, *i.e.* $C \leq 0.01$. The slope of the dashed lines can be considered as the front velocity, V_f.

Fig. 4 shows that for a constant mean viscosity and constant Re, a more viscous fluid displaces the other fluid, $m < 1$, with a thinner mixing region. By increasing m the mixing zone expands wider, and when $m > 1$, the front advances slightly faster. In our previous study, we showed that for constant displacing fluid viscosity ($\mu_{\text{eff},H}$), increasing the displaced fluid viscosity ($\mu_{\text{eff},L}$), resulting in larger m, can suppress backflow (Ghorbani et al., 2023). This observation agrees qualitatively with the observations in the current study.

The front views in Fig. 4 display a clearer interface between two fluids by increasing m. However, a clearer interface might not necessarily result in a more efficient displacement, as we can see in Fig. 4 at $m > 1$, where the displaced fluid is more viscous; here, instabilities with a clear interface have grown more non-uniformly and a bit faster along
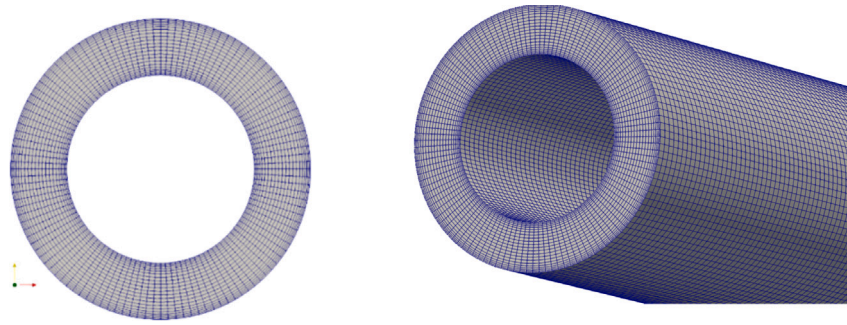
Fig. 3. The computational grid.

(a) Case 6: $m < 1$ (b) Case 10: $m = 1$ (c) Case 8: $m > 1$
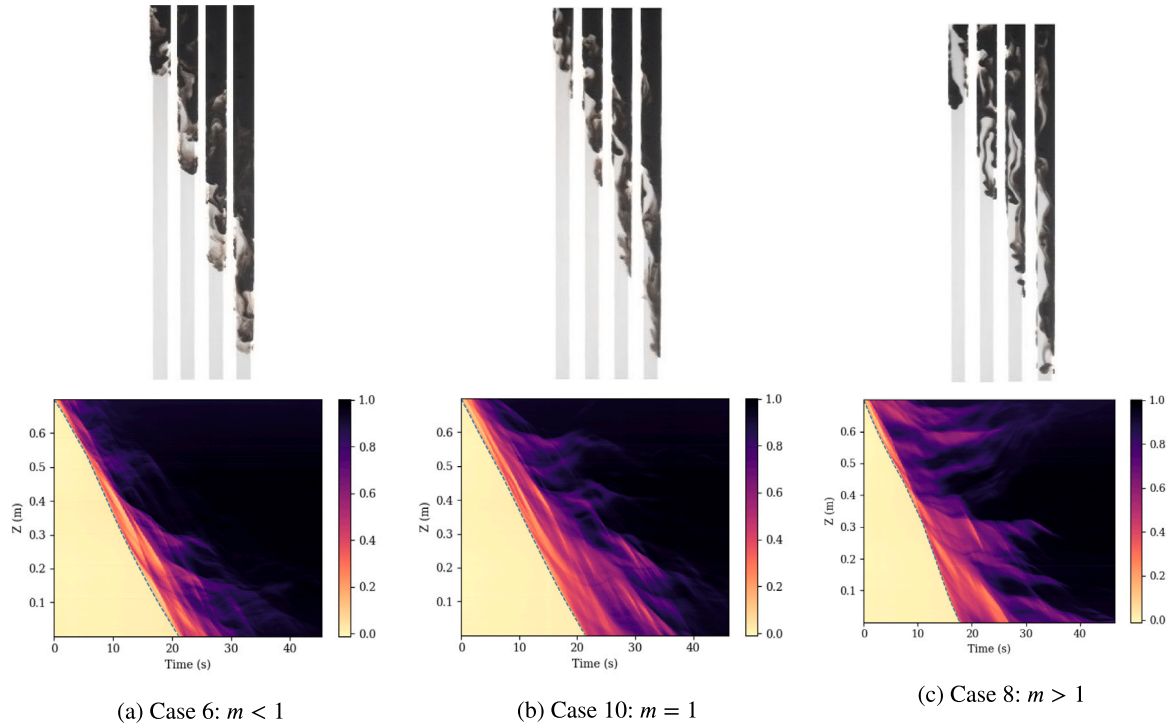
Fig. 4. Front views (top row) and spatiotemporal diagrams (bottom row) of cases 6, 10 and 8, corresponding to viscosity-stable, iso-viscous and viscosity-unstable displacements, respectively. The imposed flow velocity was in all cases 0.025 m/s.

the annulus compared to the other two cases. The dashed lines in the spatiotemporal plots show the faster movement of the front position for $m > 1$, since now the front position has reached the end of the annulus a bit earlier. We compare quantitatively the displacement efficiency of the fluids with different viscosity ratios in Fig. 5. The displacement efficiency is defined as the volume fraction occupied by *displacing* fluid inside the annulus throughout a displacement experiment and is normally evaluated as a function of time or injected fluid volume. Fig. 5 shows the displacement efficiency as a function of time for cases of 5, 7, and 9 in Table 2 on the left side, where the approximate mean viscosity is 0.0027~0.003 Pa s and the viscosity difference is about 0.008 Pa s. The plot on the right side of Fig. 5 shows the displacement efficiency for cases 1 and 3 with about 7 times higher viscosity difference, 0.014~0.019 Pa s, and a mean viscosity of approximately 0.004 Pa s. This figure indicates that for cases 5, 7, and 9, despite the different morphology of the interfaces for different viscosity hierarchies, there is no significant difference in terms of displacement efficiency, while for the higher value of the viscosity difference, the viscosity hierarchy plays a role in the efficiency of the fluids displacement. The result shows that the displacement is less efficient for case 3 $\sim$ $m > 1$ in comparison to case 1 $\sim$ $m < 1$. Our studies show the same effect of

viscosity for the higher imposed velocity. In the following sections, we investigate the effect of viscosity difference for the same viscosity hierarchy.

3.2. Effect of mean viscosity ($\bar{\mu}$) at the same viscosity hierarchy (m)

Viscosity stable displacement, $m < 1$: In this section, we present the effect of increasing the viscosity of the displacing fluid for a constant $\mu_{\text{eff},L}$ where $m \leq 1$. Fig. 6 demonstrates the results of case 1 and case 5 in Table 2. In both cases, $At = 0.003$, and the displaced fluid is water. For case 1, represented in Fig. 6(b), the displacing fluid is more viscous than the displacing fluid of case 5, shown in Fig. 6(a). It appears that increasing the viscosity difference results in less smooth displacement, as there is a wider mixing region in Fig. 6(b). To have a better view of the effect of increasing viscosity difference for viscosity stable configurations, we utilized the displacement efficiency factor. Fig. 7 illustrates the displacement efficiency of cases 5 and 1 in Fig. 7(a) and cases 6 and 2 in Fig. 7(b). This figure shows that when the displacing fluid is more viscous than the displaced fluid, increasing the viscosity of the displacing fluid does not make a significant difference in terms of displacement efficiency.
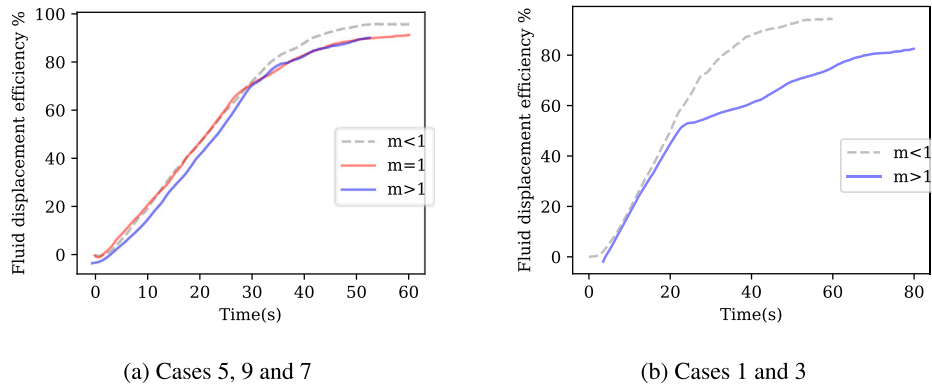
(a) Cases 5, 9 and 7   (b) Cases 1 and 3

Fig. 5. Fluid displacement efficiency for different values of m, (a): $m < 1 \sim$ case 5, $m = 1 \sim$ case 9 and $m > 1 \sim$ case 7 and (b): $m < 1 \sim$ case 1, and $m > 1 \sim$ case 3 at $V_0 = 0.012$ m/s.
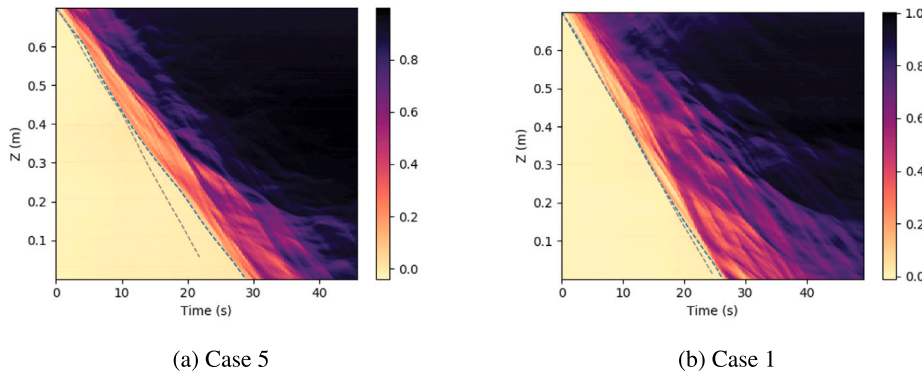

(a) Case 5   (b) Case 1

Fig. 6. Spatiotemporal plots of density unstable fluids displacement in a vertical annulus at $At = 0.003$ at $V_0 = 0.012$ m/s for (a) $m = 0.12 \sim$ case 5, and (b) $m = 0.05 \sim$ case 1 in Table 2. ($\mu_{\mathrm{eff},L_a} = \mu_{\mathrm{eff},L_b}$ and $\mu_{\mathrm{eff},H_a} < \mu_{\mathrm{eff},H_b}$). The blue dashed curve represents the front position in the experimental results, and the gray dashed curve shows the front position from the simulations.
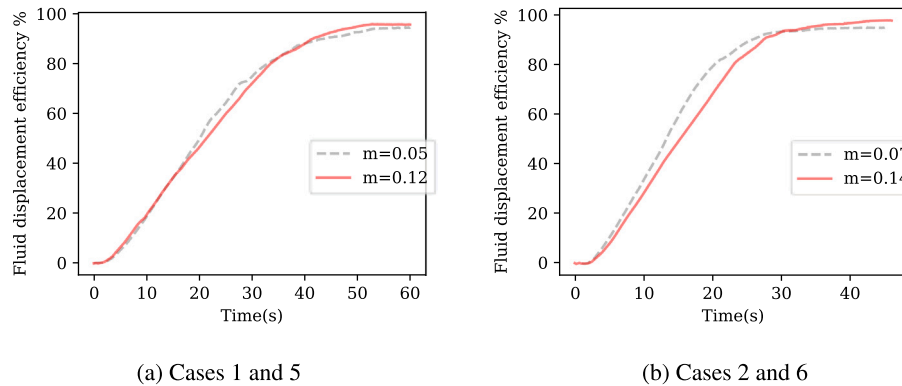

(a) Cases 1 and 5   (b) Cases 2 and 6

Fig. 7. Displacement efficiency for the displacement in a vertical annulus at $At = 0.003$. In all cases $m < 1$ and in (a) $V_0 = 0.012$ m/s, red curve: case 5 and dashed curve: case 1, in (b) $V_0 = 0.025$ m/s, red curve: case 6 and dashed curve: case 2. The displaced fluids for all cases are similar and the displacing fluid of cases represented by gray dashed curves is more viscous than the cases in red color.

Viscosity unstable displacement, $m > 1$: In the following, we examine the effect of increasing m for a constant $\mu_{\mathrm{eff},H}$, where $m \geq 1$. In Fig. 8, the results of case 7 and case 3 in Table 2 are presented. In both cases, the density difference is the same with the similar properties of the displacing fluid, while in case 3 (Fig. 8b), the displaced fluid is more viscous than the displaced fluid of case 7 (Fig. 8a). Comparing Fig. 8a and b shows that although increasing the $\mu_{\mathrm{eff},L}$ leads to lower Re, it does not result in smoother displacement. By increasing the viscosity of the displaced fluid, the instabilities grow faster, leading to higher front velocity. The dashed curves represent the front position from the experiments and the numerical simulations. The results of the numerical simulation will be discussed in Section 4 in detail.

Using the fluid displacement efficiency, Fig. 9 quantifies the effects of increasing the viscosity of the displaced fluid. In each plot, the higher value of m corresponds to a larger viscosity of the displaced fluid. It is evident that larger viscosities of the displaced fluids result in less efficient displacement, as the dashed curves deviate from the linear trend earlier and end up at a lower maximum value. Comparing Figs. 7 and 9 indicates that changing the viscosity ratio for viscosity unstable configuration has a stronger effect on the displacement.

4. Numerical results

We next discuss results from numerical simulations of the reverse-circulation displacements listed in Table 2, and compare qualitatively
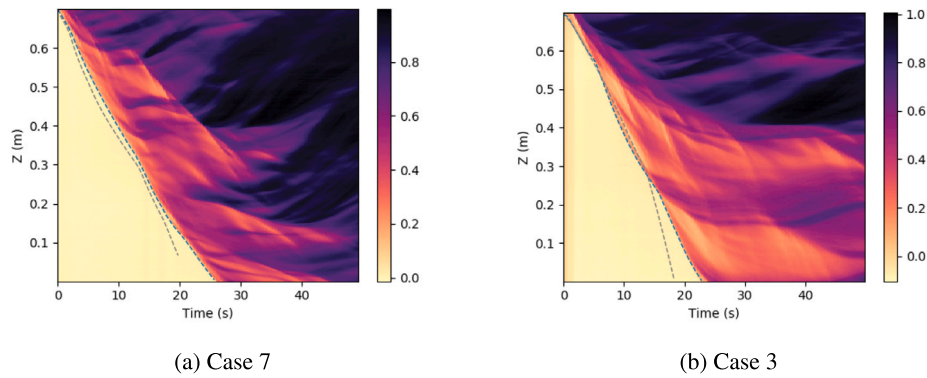
(a) Case 7   (b) Case 3

Fig. 8. Spatiotemporal plots of density unstable fluids displacement in a vertical annulus at $At = 0.003$ at $V_0 = 0.012$ m/s for (a) $m = 9.5 \sim$ case 7, and (b) $m = 23 \sim$ case 3 in Table 2. ($\mu_{\mathrm{eff},H_a} = \mu_{\mathrm{eff},H_b}$ and $\mu_{\mathrm{eff},L_a} < \mu_{\mathrm{eff},L_b}$). The blue dashed curve represents the front position in the experimental results, and the gray dashed curve shows the front position from the simulations.
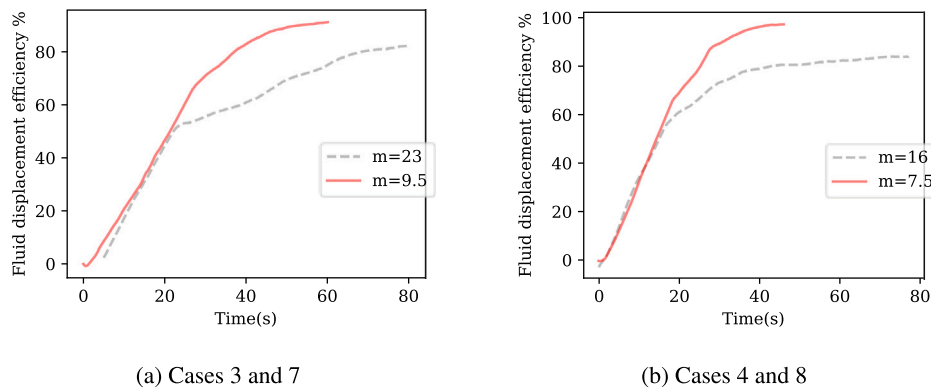

(a) Cases 3 and 7   (b) Cases 4 and 8

Fig. 9. Displacement efficiency for the displacement in a vertical annulus at $At = 0.003$. In all cases $m > 1$ and in (a) $V_0 = 0.012$ m/s, red curve: case 7 and dashed curve: case 3, in (b) $V_0 = 0.025$ m/s, red curve: case 8 and dashed curve: case 4. The displacing fluids for all cases are similar, and the displaced fluid of cases represented by gray dashed curves is more viscous than the cases in red color.

to the corresponding experimental observations. Numerical results based on cases 5, 7, and 9 are shown in Fig. 10; cases 5, 7, and 9 correspond to density-unstable displacements where $Re \approx 30$, and where the viscosity ratio is $m < 1$ (viscosity-stable), $m > 1$ (viscosity-unstable), and $m \approx 1$ (iso-viscous), respectively. In Fig. 10, each case is illustrated using a "front view" of the displacement process (top row), the corresponding spatiotemporal diagram (cross-sectional average of concentration; middle row), and in terms of cross-sectional average concentration scaled according to a similarity variable $x = (z - V_0 t)/\sqrt{t}$. The latter presentation form is used to assess whether the mixing region between the two fluids grows according to a diffusive scaling of position and time, as seen by an observer that translates in the downward direction (along the annulus) at the imposed flow speed. Previous research involving density-unstable and iso-viscous downward displacements in tubes has shown that experiments that have $Re/Fr \geq 500 - 50Fr$ exhibit such diffusive scaling of the fluid mixing region in pipe geometries (Alba et al., 2013). Now, cases 5, 7, and 9 all have $Re \approx 30$ and $Fr = 0.04$, for which the criterion indeed suggests diffusive scaling.

The top row in Fig. 10 suggests interface mixing that agrees qualitatively with similar experiments, such as those shown in Fig. 4, namely pronounced buoyancy-driven instability combined with the tendency of fingers of the displacing fluid penetrating the displaced fluid when $m > 1$ (viscosity-unstable configuration). This observation also agrees qualitatively with recent reverse-circulation displacement experiments in annular geometries (Eslami et al., 2022). In the spatiotemporal diagrams (middle row) of Fig. 10, two dashed curves are added to each diagram; these correspond to the front position of the interfacial mixing region as obtained experimentally and as predicted by numerical simulation. In all cases, we observe a satisfactory agreement between

experiment and simulation, although with the front advancing slightly slower in experiments. From the spatiotemporal diagrams, we also note that *breakthrough* of displacing fluid at the outlet ($Z = 0$ m) occurs at nearly the same instance in simulations, although the viscosity-stable case ($m < 1$) exhibits a slight delay compared to the other two cases (a few seconds, at most). The concentration map shown in the spatiotemporal diagrams indicates improved displacement efficiency when $m < 1$ (case 5), and that the viscosity-unstable case is the least efficient, as expected.

The scaled concentration profiles shown in the bottom row of Fig. 10 are extracted from the spatiotemporal diagrams (i.e. the concentration profiles correspond to the data along discrete vertical lines in the spatiotemporal diagrams) *before* the displacing fluid breaks through at the outlet. The black solid curve corresponds to $c(x, t) = (1/2)\mathrm{erfc}(x/\sqrt{4Dt})$, where erfc() denotes the complementary error function. This form for c corresponds to the analytical solution of a one-dimensional diffusion problem, with D interpreted as a "macroscopic" diffusion coefficient (Crank, 1975; Alba et al., 2013). We observe a better match between the characteristic diffusion solution and the numerical results at $m < 1$, i.e. the viscosity-stable configuration. Transitioning to the viscosity-unstable configuration, i.e. $m > 1$, the mixing region evolves according to an "inertial" classification (Alba et al., 2013; Ghorbani et al., 2023). We consider this observation interesting, as it suggests that the displacement regime classification is also dependent on the viscosity ratio of the two fluids.

Finally, in Fig. 11 we provide a 3D view of the displacement of cases 1 and 3. This 3D view shows the stronger transverse flow for the viscosity stable displacement and faster growth of instabilities for the viscosity unstable displacement; as we can see for case 1 with $m < 1$ the fluid is more distributed around the annulus with lower velocity
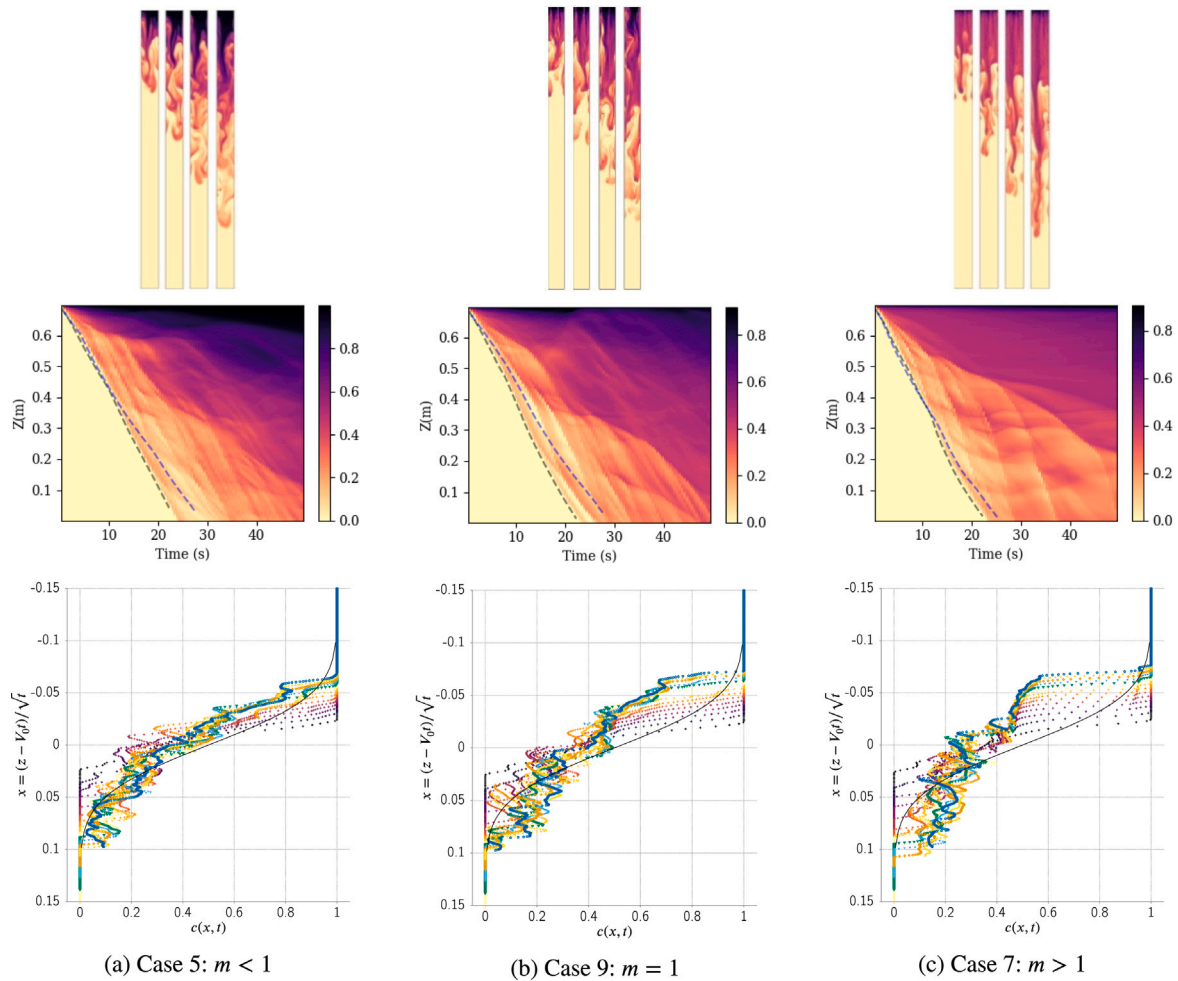
Fig. 10. Comparison of numerical results for cases 5, 7, and 9, corresponding to $Re \approx 30$, $Fr = 0.04$ and viscosity ratios $m < 1$, $m > 1$ and $m = 1$, respectively. The top row presents the frontal view of the annulus, mimicking a camera that images one side of the annulus. The four snapshots are spaced by 5 s. The middle row presents the corresponding spatiotemporal diagrams, where the 3D concentration profile in simulations has been averaged over the annulus cross-section. The bottom row shows the cross-sectional averaged concentration profiles at selected times before displacing fluid reaches the outlet and scales the position coordinate according to a "diffusive" similarity variable x.

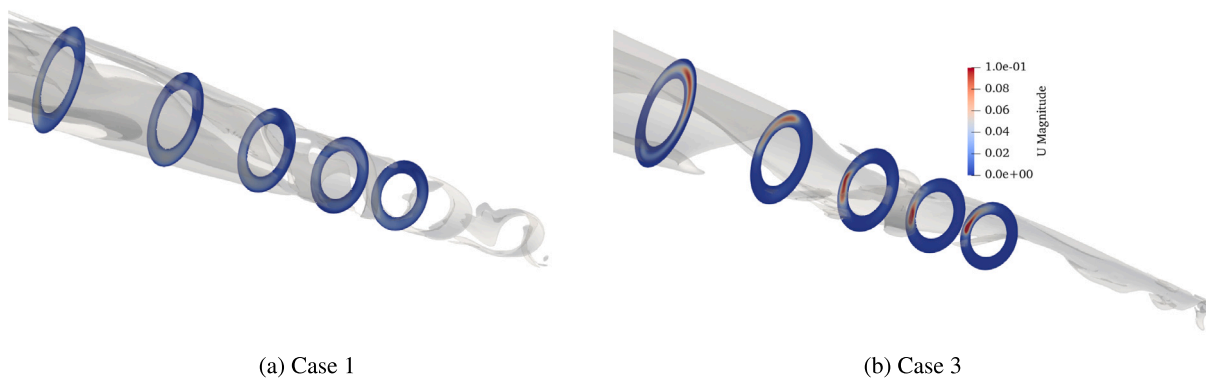**Fig. 11.** 3D view of the fluid displacement for viscosity-stable (a) and viscosity-unstable (b) cases.

$(0 < U < 0.035$ m/s$)$ in comparison to the other case with $m > 1$, where the fluid moves faster $(0 < U < 0.1$ m/s$)$ from one side.

Effect of inclination: In practice, the casing is not perfectly vertical. We utilized the numerical model to study the effect of viscosity hierarchy on the fluid displacement in the annulus with an inclination of 20°. The fluid properties were considered the same as Table 1. The purpose is to investigate whether the geometry can amplify the effect of the viscosity hierarchy. We employed the fluid efficiency parameter

to quantify the effect of inclination and compare the results with the vertical annuli. In Fig. 12, we plot the fluid displacement efficiency for two values of viscosity difference with different viscosity hierarchies. In plot (b), the viscosity difference between fluids is larger than plot (a). The mean viscosity of the different cases presented in each plot is the same. Due to inclination and gravity, the fluid flow tends to the lower side of the annulus, resulting in nonuniform displacement of the fluid around the annulus. As a result, less efficient displacement is expected
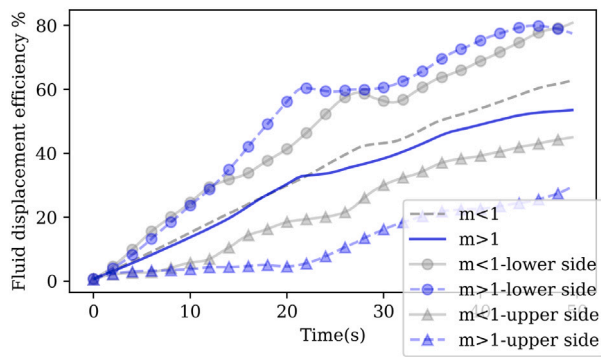
(a) Cases 5 and 7
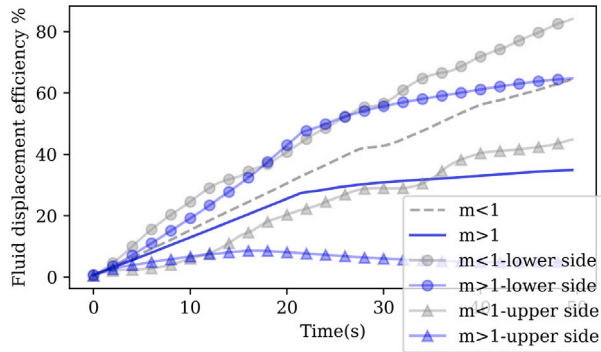
(b) Cases 1 and 3

Fig. 12. Fluid displacement efficiency from the numerical simulations for different values of m, (a): $m < 1 \sim$ case 5, and $m > 1 \sim$ case 7 and (b): $m < 1 \sim$ case 1, and $m > 1 \sim$ case 3 at $V_0 = 0.012$ m/s in the inclined annulus.

Fig. 13. Density-unstable displacement from 3D numerical simulations in the inclined annulus with the angle of 20° with the fluid properties as case 3, the letters 'L' and 'U' represent the lower and the upper sides of the annulus.

Table 3
Main dimensionless numbers for comparison of full-scale displacement conditions and the current study.

Quantity	Full-scale value	Current study
Annulus aspect ratio, κ	0.72	0.63
Inclination	2–6°	0°
Eccentricity	≈ 0.7	0
Atwood number, At	0.022	0.003
Reynolds number, Re	283	18.84–71.42
Densimetric Froude number, Fr^2	26	0.002–0.008
$\chi = 2Re/Fr^2$	21.7	10^3–10^4
Viscosity ratio, m	?	0.05–22.88

on the upper side of the annulus. In Fig. 12, beside the total fluid displacement efficiency, we extracted the displacement efficiency in the top half of the annulus and the lower half of the annulus. Comparing Figs. 5 and 12a shows that the effect of the viscosity hierarchy is stronger in inclined annuli in comparison to vertical ones, as case 7 in Fig. 12a has less efficient displacement in comparison to other cases. The displacement efficiency of the upper/lower sides of the annulus illustrates clearly how a more viscous displaced fluid results in less efficiency in the upper side of the annulus. This effect gets significantly stronger for the higher viscosity difference. Fig. 12b shows that for case 3, the displacement efficiency on the upper side is close to zero. The poor displacement of the fluid for case 1 in the upper side of the inclined annulus is shown in Fig. 13. This figure illustrates a 3D view of the fluid displacement in the inclined annulus over time for case 3. The letters "L" and "U" represent the lower and upper halves of the annulus.

5. Discussion

We next address the similarity of the current laboratory-scaled investigation to field-scale density-unstable displacements, using the dimensionless numbers (or Π-groups) identified in Section 2.1.2. Physical similarity requires that all these numbers (or groups) for the downscaled model and the full-scale (prototype) model are equal (Barenblatt, 2003). We use the reverse-circulation cementing operation discussed by Skadsem et al. (2021) and Skadsem and Kragset (2022) as the basis for establishing relevant full-scale dimensionless numbers, as specified in Table 3. This full-scale case is based on the reverse-circulation displacement of an 1820 kg/m³ drilling fluid/spacer by a 1900 kg/m³ cement slurry in the annulus between a 9 5/8-in production casing and
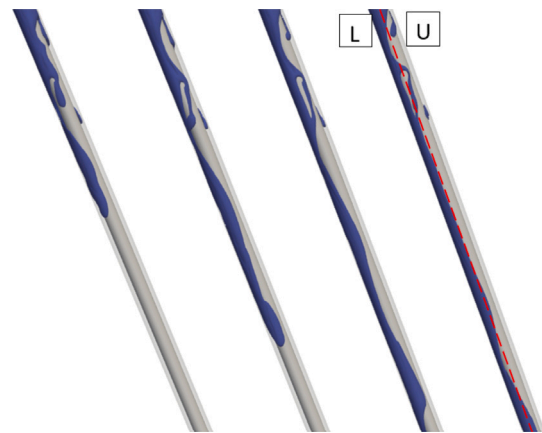
a 13 3/8-in intermediate casing. Lacking detailed viscosity characterization of the involved fluids as well as specific pumping rates, Skadsem and Kragset (2022) assumed a constant cement slurry viscosity of 0.1 Pa s and an imposed flow rate of 800 l/min, based on the original cementing report (from 1985). The reverse-circulation operation was performed as a second-stage cementing job, where the formation above a weak open-hole zone was cemented by bullheading from the surface. The retrieved sections confirm a fully eccentric annulus, where the stand-off is due to the outer diameter of the 9 5/8-in casing collars resting on the inner wall of the 13 3/8-in casing, even if the sections were retrieved from a near-vertical part of the wellbore. The dimensionless numbers listed in Table 3 suggest "laminar" flowing conditions in the full-scale case and that inertia was important relative to buoyancy ($Fr^2 = 26$). Furthermore, buoyant and viscous stresses were comparable ($\chi = 21.7$, suggesting no back-flow of lighter fluid Amiri et al., 2016; Skadsem and Kragset, 2022). We note that the permeability of the hardened cement was measured to have permeability ranging from micro- to millidarcies (Skadsem, 2022), and was, as such comparable to that of other wells exhibiting sustained casing pressure (Stormont et al., 2018).

Compared to this field case, the current study has employed a smaller density difference relative to the mean fluid density, as expressed by the Atwood number. Indeed, $At = 0.003$ is equivalent to a 1900 kg/m³ cement slurry displacing a drilling fluid/spacer of density 1888 kg/m³; compared to typical density differences between cementing fluids, this density difference is considered relatively small. Still, the effect of buoyancy is pronounced in our experiments and simulations, as expressed by the small densimetric Froude number, $Fr^2 = 0.002–0.008$, and by the relatively large value of χ, which expresses the ratio of buoyant stresses to viscous stresses. As such, buoyancy plays a dominant role in our experiments, and probably more so than in the full-scale example discussed above. A reduction in the density difference (or equivalently, an increase in fluid viscosity

and imposed flow velocity) is expected to stabilize the displacements considered above and reduce the tendency for the lighter fluid to backflow (*i.e.* to flow in the opposite direction of the imposed flow). Our study therefore highlights how the viscosity hierarchy can improve the displacement efficiency under significantly density-unstable conditions. Finally, one can expect that a large portion of the annular space will, in practice, be fully eccentric, with casing stand-offs determined by the inner casing collar diameter. Although our study does not consider eccentricity, its effect is expected to be similar to that of inclination, as studied numerically above. That is, a preferred flow path will promote the downward flow of dense, displacing fluid (along the wide sector of the annulus for eccentric cases, along the low side of an inclined, concentric annulus). Both cases are expected to produce more challenging displacement conditions compared to the perfectly vertical-concentric arrangement studied experimentally above. Interestingly, the combination of eccentricity and inclination can improve the balance of gravity and geometry/eccentricity, provided the inner casing is offset towards the low side of the wellbore.

6. Summary and conclusion

This study has explored the effect of viscosity hierarchy on the efficiency of annular reverse-circulation displacements, with a particular emphasis on primary cementing operations. The main thrust of this study has been to assess how the viscosity hierarchy between density-unstable fluid pairs impacts displacement efficiency, with a focus on vertical and inclined wellbore configurations. We expand upon previous studies of downward annular displacements by considering fluid pairs that provide fixed mean viscosity and either viscosity-stable or -unstable conditions.

Experiments and numerical simulations of the displacement cases exhibited unstable flow patterns reminiscent of the classical Rayleigh–Taylor instability and signs of viscous-fingering for the viscosity-unstable cases. The unstable displacements are characterized by a mixing region with fluctuating spatiotemporal concentration levels and a front position that propagates considerably faster than the imposed flow velocity. Further, the numerical simulations indicate that a mild inclination (20°) will significantly impact the displacement, with the dense, displacing fluid flowing predominantly along the low side of the annulus (stratification). While all fluid and displacement configurations in this study produced significant instabilities, we observed that increasing the viscosity of the displacing fluid suppresses fingering patterns and results in a more diffusive mixing region. Simultaneous density-unstable and viscosity-unstable configurations are particularly prone to exhibit poor displacement efficiency, as expected. As such, our study suggests that the conventional circulation guideline involving the viscosity ratio of the two fluids (or more precisely, the friction pressure gradients Couturier et al., 1990) can be carried over to reverse-circulation displacements. In our experiments, the destabilizing density difference was not fully compensated by the viscosity ratio, but we observed that the viscosity ratio between the fluids impacted the mixing zone between the fluids and that viscosity-stable conditions suppressed finger growth. Our work therefore suggests that maintaining viscosity-stable configurations can be beneficial for buoyant reverse-circulation displacements.

Although the downscaled laboratory experiments do not achieve dynamic similarity compared to the considered field case, we consider the effect of viscosity ratio on displacement efficiency to still be reflected in our experiments and simulations. For future research, we consider the effects of casing eccentricity to be particularly relevant, especially since casing strings are not centralized over the full length. We expect that eccentricity will mainly act to destabilize the interface and promote advancements of the dense fluid along the wide sector of the annulus in vertical annuli. Future work should assess whether the potentially detrimental effects of eccentricity can be mitigated through fluid viscosity and/or the imposed flow rate. Further insights could

also motivate the placement of casing centralizers closer to the surface and in near-vertical parts of the well in cases where reverse-circulation cementing is planned. Of further interest would also be to assess quantitative criteria for the onset of backflow of the lighter fluid, as well as the existence of possible steady (buoyant) displacements. Finally, future work should also attempt to improve scaling relative to field conditions and, where possible, also analyze actual reverse-circulation jobs from the field using available cementing logs and operational data.

CRediT authorship contribution statement

Maryam Ghorbani: Writing – review & editing, Writing – original draft, Visualization, Validation, Methodology, Investigation, Formal analysis, Conceptualization. **Knut Erik Teigen Giljarhus:** Writing – review & editing, Validation, Investigation, Formal analysis. **Hans Joakim Skadsem:** Writing – review & editing, Visualization, Supervision, Investigation, Funding acquisition, Conceptualization.

Declaration of competing interest

The authors declare that they have no known competing financial interests or personal relationships that could have appeared to influence the work reported in this paper.

Data availability

Data will be made available on request.

References

Abedi, B., Berghe, L.S., Fonseca, B.S., Rodrigues, E.C., Oliveira, R.M., de Souza Mendes, P.R., 2022. Influence of wall slip in the radial displacement of a yield strength material in a Hele–Shaw cell. Phys. Fluids 34 (11), 113102. http://dx.doi.org/10.1063/5.0128287.

Alba, K., Taghavi, S.M., Frigaard, I.A., 2013. Miscible density-unstable displacement flows in inclined tube. Phys. Fluids 25 (6), 067101. http://dx.doi.org/10.1063/1.4808113.

Amiri, A., Larachi, F., Taghavi, S.M., 2016. Buoyant miscible displacement flows in vertical pipe. Phys. Fluids 28 (10), 102105. http://dx.doi.org/10.1063/1.4965250.

Barenblatt, G.I., 2003. Scaling. In: Cambridge Texts in Applied Mathematics, Cambridge University Press.

Beltrán-Jiménez, K., Gardner, D., Kragset, S., Gebremariam, K.F., Reales, O.A.M., Minde, M.W., de Souza, M.I.L., Aasen, J.A., Skadsem, H.J., Delabroy, L., 2022. Cement properties characterization from a section retrieved from an oil production well after 33 years of downhole exposure. J. Pet. Sci. Eng. 208, 109334. http://dx.doi.org/10.1016/j.petrol.2021.109334.

Bird, R.B., Armstrong, R.C., Hassager, O., 1987. Dynamics of Polymeric Liquids: Volume 1 - Fluid Mechanics, second ed. John Wiley & Sons.

Bour, D.L., Hodson-Clarke, A., Russell, P., 2013. First reverse circulation cement job in Australia executed in HP-HT geothermal well in cooper basin. In: SPE Asia Pacific Unconventional Resources Conference and Exhibition. pp. 1–13. http://dx.doi.org/10.2118/167067-MS, SPE-167067-MS.

Couturier, M., Guillot, D., Hendriks, H., Callet, F., 1990. Design rules and associated spacer properties for optimal mud removal in eccentric annuli. In: PETSOC Annual Technical Meeting, Vol. PETSOC-90-112. pp. 1–8. http://dx.doi.org/10.2118/90-112.

Crank, J., 1975. The Mathematics of Diffusion, second ed. Clarendon Press.

Davies, J., Parenteau, K., Schappert, G., Tahmourpour, F., Griffith, J., 2004. Reverse circulation of primary cementing jobs—Evaluation and case history. In: SPE/IADC Drilling Conference and Exhibition. pp. 1–8. http://dx.doi.org/10.2118/87197-MS, SPE-87197-MS.

Debacq, M., Fanguet, V., Hulin, J.P., Salin, D., Perrin, B., 2001. Self-similar concentration profiles in buoyant mixing of miscible fluids in a vertical tube. Phys. Fluids 13 (11), 3097–3100. http://dx.doi.org/10.1063/1.1405442.

Eslami, A., Akbari, S., Taghavi, S., 2022. An experimental study of displacement flows in stationary and moving annuli for reverse circulation cementing applications. J. Pet. Sci. Eng. 213, 110321. http://dx.doi.org/10.1016/j.petrol.2022.110321.

Etrati, A., Alba, K., Frigaard, I.A., 2018. Two-layer displacement flow of miscible fluids with viscosity ratio: Experiments. Phys. Fluids 30 (5), 052103. http://dx.doi.org/10.1063/1.5026639.

Etrati, A., Frigaard, I.A., 2018. Viscosity effects in density-stable miscible displacement flows: Experiments and simulations. Phys. Fluids 30 (12), 123104. http://dx.doi.org/10.1063/1.5065388.

Fjær, E., Holt, R.M., Horsrud, P., Raaen, A.M., 2008. Petroleum Related Rock Mechanics. Elsevier.

Friðleifsson, G.Ó., Elders, W.A., Zierenberg, R.A., Stefánsson, A., Fowler, A.P.G., Weisenberger, T.B., Harðarson, B.S., Mesfin, K.G., 2017. The Iceland Deep Drilling Project 4.5 km deep well, IDDP-2, in the seawater-recharged Reykjanes geothermal field in SW Iceland has successfully reached its supercritical target. Sci. Drill. 23, 1–12. http://dx.doi.org/10.5194/sd-23-1-2017.

Ghorbani, M., Royaei, A., Skadsem, H.J., 2023. Reverse circulation displacement of miscible fluids for primary cementing. J. Energy Resour. Technol. 145 (7), 073101.

Grant, L., Japar, N.J., Reagins, D., Hale, A., Mercado, S., van den Haak, A.L., Lloyd, R., Pereira, A.G., 2014. Proactive novel approach and design strategies to zonal isolation in a highly challenging deep water environment. In: SPE Annual Technical Conference and Exhibition. pp. 1–14. http://dx.doi.org/10.2118/170977-MS, SPE-170977-MS.

Hernandez, R., 2012. Unconventional cementing method enables drilling in lost-circulation zones: Case history. In: SPE Asia Pacific Oil and Gas Conference and Exhibition. pp. 1–6. http://dx.doi.org/10.2118/154564-MS, SPE-154564-MS.

Hernández, R., Bour, D., 2010. Reverse-circulation method and durable cements provide effective well construction: A proven technology. In: Thirty-Fifth Workshop on Geothermal Reservoir Engineering. pp. 1–4.

MacEachern, D., Cowan, M., Harris, K., Faul, R., 2003. Reverse foam cementing an offshore production tieback. In: AADE 2003 National Technology Conference "Practical Solutions for Drilling Challenges". pp. 1–14, AADE-03-NTCE-32.

Macfarlan, K.H., Wreden, C.P., Schinnell, M.J., Nikolaou, M., 2017. A comparative hydraulic analysis of conventional- and reverse-circulation primary cementing in offshore wells. SPE Drill. Complet. 32 (01), 59–68. http://dx.doi.org/10.2118/185165-PA.

Marquairi, R., Brisac, J., 1966. Primary cementing by reverse circulation solves critical problem in the North Hassi-Messaoud Field, Algeria. J. Pet. Technol. 18 (02), 146–150. http://dx.doi.org/10.2118/1111-PA.

Marriott, T., Chase, S., Khallad, I., Bolt, R., Whelan, P., 2007. Reverse-circulation cementing to seal a tight liner lap. In: OTC Offshore Technology Conference. pp. 1–10. http://dx.doi.org/10.4043/18839-MS, OTC-18839-MS.

McNerlin, B., Gao, Q., Mohiuldin, G., Oakey, N., 2013. Open hole fluid displacement analysis - forward vs. Reverse circulations. In: SPE Annual Technical Conference and Exhibition, New Orleans, Louisiana, USA, September 2013. pp. 1–17. http://dx.doi.org/10.2118/166359-MS, SPE-166359-MS.

Moore, R., Bour, D., Reed, S., Hernandez, R., 2005. High-temperature wells with lost-circulation demands and reverse-circulation techniques using foamed-cement systems: Two case histories. SPE Drill. Complet. 20 (02), 133–140. http://dx.doi.org/10.2118/84563-PA.

Murdoch, E., Valverde, E., Sharma, R., Wreden, C., Goodwin, A., Osei-Kuffour, J., Kimmitt, K., Loonstra, C., Ghaempanah, B., Reagins, D., 2016. Leveraging RFID technology for deepwater drilling and completions challenges. In: SPE Intelligent Energy International Conference and Exhibition. pp. 1–29. http://dx.doi.org/10.2118/181012-MS, SPE-181012-MS.

Nelson, E., Guillot, D., 2006. Well Cementing. Schlumberger.

Pelipenko, S., Frigaard, I.A., 2004. Visco-plastic fluid displacements in near-vertical narrow eccentric annuli: prediction of travelling-wave solutions and interfacial instability. J. Fluid Mech. 520, 343–377. http://dx.doi.org/10.1017/S0022112004001752.

Pelton, B., Adam, D., Granier, G., Turner, W., Tellez, D., Willis, J., 2023. Unconventional bradenhead cementing in the delaware basin case history. SPE Drill. Complet. 38 (01), 110–119. http://dx.doi.org/10.2118/208756-PA.

Reagins, D., Herr, D., Jee, B., Ownby, J., Duthie, J., Giroux, R., Kendziora, L., 2016. Development of a subsurface reverse circulation tool system to cement weak and depleted zones in deepwater formations. In: SPE Annual Technical Conference and Exhibition. pp. 1–20. http://dx.doi.org/10.2118/181482-MS, SPE-181482-MS.

Skadsem, H.J., 2022. Characterization of annular cement permeability of a logged well section using pressure–pulse decay measurements. J. Energy Resour. Technol. 144 (5), 053004. http://dx.doi.org/10.1115/1.4053709.

Skadsem, H.J., Gardner, D., Beltrán-Jiménez, K., Govil, A., Palacio, G.O., Delabroy, L., 2021. Study of ultrasonic logs and seepage potential on sandwich sections retrieved from a North Sea production well. SPE Drill. Complet. 36 (04), 976–990. http://dx.doi.org/10.2118/206727-PA, SPE-206727-PA.

Skadsem, H.J., Kragset, S., 2022. A numerical study of density-unstable reverse circulation displacement for primary cementing. J. Energy Resour. Technol. 144 (12), 123008. http://dx.doi.org/10.1115/1.4054367.

Skadsem, H.J., Leulseged, A., Cayeux, E., 2019. Measurement of drilling fluid rheology and modeling of thixotropic behavior. Appl. Rheol. 29 (01), 1–11. http://dx.doi.org/10.1515/arh-2019-0001.

Stormont, J.C., Fernandez, S.G., Taha, M.R., Matteo, E.N., 2018. Gas flow through cement-casing microannuli under varying stress conditions. Geomech. Energy Environ. 13, 1–13. http://dx.doi.org/10.1016/j.gete.2017.12.001.

Tehrani, M.A., Bittleston, S.H., Long, P.J.G., 1993. Flow instabilities during annular displacement of one non-Newtonian fluid by another. Exp. Fluids 14, 246–256. http://dx.doi.org/10.1007/BF00194015.

Turki, W., Mackay, A., 1983. Primary cementing across massive lost circulation zones. In: SPE Middle East Oil and Gas Show and Conference. pp. 409–416. http://dx.doi.org/10.2118/11490-MS, SPE-11490-MS.

Wreden, C., Watters, J.T., Giroux, R., Nikolaou, M., Macfarlan, K., Richardson, D.A., 2014. Deepwater reverse-circulation primary cementing: Applicability and technical path forward for implementation. In: OTC Offshore Technology Conference. pp. 1–19. http://dx.doi.org/10.4043/25194-MS, OTC-25194-MS.